

# Mean Structure of Tropical Cyclones Making Landfall in Mainland China

BAI Lina<sup>1\*</sup> (白莉娜), YU Hui<sup>1</sup> (余 晖), XU Yinglong<sup>2</sup> (许映龙), and WANG Yuan<sup>3</sup> (王 元)

<sup>1</sup> *Laboratory of Typhoon Forecast Technique, Shanghai Typhoon Institute, China Meteorological Administration (CMA), Shanghai 200030*

<sup>2</sup> *National Meteorological Center, CMA, Beijing 100081*

<sup>3</sup> *Key Laboratory of Mesoscale Severe Weather of Ministry of Education, Nanjing University, Nanjing 211102*

(Received November 13, 2013; in final form March 14, 2014)

## ABSTRACT

The mean kinematic and thermodynamic structures of tropical cyclones (TCs) making landfall in mainland China are examined by using sounding data from 1998 to 2009. It is found that TC landfall is usually accompanied with a decrease in low-level wind speed, an expansion of the radius of strong wind, weakening of the upper-level warm core, and drying of the mid-tropospheric air. On average, the warm core of the TCs dissipates 24 h after landfall. The height of the maximum low-level wind and the base of the stable layer both increase with the increased distance to the TC center; however, the former is always higher than the latter. In particular, an asymmetric structure of the TC after landfall is found. The kinematic and thermodynamic structures across various areas of TC circulation differ, especially over the left-front and right-rear quadrants (relative to the direction of TC motion). In the left-front quadrant, strong winds locate at a smaller radius, the upper-level temperature is warmer with the warm core extending into a deep layer, while the wet air occupies a shallow layer. In the right-rear quadrant, strong wind and wet air dwell in an area that is broader and deeper, and the warmest air is situated farther away from the TC center.

**Key words:** landing tropical cyclone, kinematic structure, thermodynamic structure, asymmetric structure

**Citation:** Bai Lina, Yu Hui, Xu Yinglong, et al., 2014: Mean structure of tropical cyclones making landfall in mainland China. *J. Meteor. Res.*, **28**(3), 407–419, doi: 10.1007/s13351-014-3060-4.

## 1. Introduction

The landfall process of tropical cyclones (TCs) is an important research topic because landfalling TCs usually damage coastal areas through severe winds, intense rainfall, and hazardous storm surges, resulting in numerous casualties and great economic losses. Observational studies (Powell, 1987; Powell and Houston, 1998; Blackwell, 2000; Chan et al., 2004) and numerical simulations (Tuleya et al., 1984; Wong and Chan, 2007; Ramsay et al., 2009) have shown that the different forcing of land and ocean creates strong asymmetric structures within TCs. These asymmetries may affect not only the intensity and motion of TC (Mont-

gomery and Kallenbach, 1997; Wang, 2002; Wong and Chan, 2006; Szeto and Chan, 2010; Chambers and Li, 2011), but also its precipitation distribution and wind gusts (Powell, 1987; Powell and Houston, 1998). Therefore, understanding the kinematic and thermodynamic structures of TCs that form during the TC landfall process is vital to improvement of TC forecasting and warning.

Numerous observational studies and numerical simulations have documented the differences in the wind distributions of TCs before and after landfall as a result of increased roughness over land. Tuleya and Kurihara (1978) indicated that the contrasting roughness between land and sea generates a quasi-steady

Supported by the National Basic Research and Development (973) Program of China (2009CB421500), National Natural Science Foundation of China (40730948, 40921160381, 41275057, 41275067, and 41305049), and China Meteorological Administration Special Public Welfare Research Fund (GYHY201006008 and GYHY200906002).

\*Corresponding author: bailn@mail.typhoon.gov.cn.

©The Chinese Meteorological Society and Springer-Verlag Berlin Heidelberg 2014

convergence (divergence), along with negative (positive) relative vorticity zones along the coastline where the flow is onshore (offshore). Powell (1987) emphasized that wind asymmetry is caused by the combined effects of roughness variations between land and sea, environmental flow in the background, and flow translation. Kepert (2006a, b) studied hurricanes Georges and Mitch and noted the differences between the asymmetric structure produced by the landfall process and motion-induced asymmetry. For instance, the motion-induced asymmetry is discontinuous and much stronger than the asymmetry induced by landfall. Wong and Chan (2007) simulated the pre-landfall, landfall, and post-landfall wind distributions of TCs and concluded that the asymmetry of surface wind in the pre- (post-) landfall position is related to the acceleration (deceleration) of the flow over the sea (land). Ramsay et al. (2009) simulated TC Larry, and their results support the findings of earlier studies, which state that frictional convergence in the boundary layer is significant in determining asymmetrical structures of TCs.

Another important process is the entrainment of dry and cool air into TC circulation. Studies (Tuleya and Kurihara, 1978; Powell, 1987) suggested that losses in oceanic heat and moisture source cool the middle levels of the TC circulation, in combination with the advection of dry air from land; subsequently, TC intensity reduces. Knupp et al. (2006) reported that before TC Gabrielle landed, stratiform rain over the land established a mesoscale region of cool air (2001). Rebecca and Gray (2005) derived the strong asymmetry of the landfalling Hurricane Bonnie (1998), which depicts that the equivalent potential temperature in the southern portion of the eyewall decreases, the air in the right-rear quadrant is cool, and the inflow of the circulation center in the southeast is strong.

Observing the detailed structure of a TC is challenging; thus, most previous investigations are in the form of case studies of individual storms. Nevertheless, the variability in the TC structure is in no doubt great, and no single TC can represent a generic cyclone. Therefore, a study that examines the general features of landfalling TCs with multiple cases is

highly desirable. The current study aims to obtain the generic kinematic and thermodynamic characteristics of TCs that have made landfall in mainland China, along with the evolution of these characteristics in the landfall process. Section 2 details the dataset used in this study. After analyzing the sounding data, the results about the kinematic structure of landing TCs are presented in Section 3. Observations of the thermodynamic structures of these TCs are analyzed in Section 4. The study is then summarized and discussed in Section 5.

## 2. Data and method

### 2.1 Data

TC intensity and location data from 1998 to 2009 are extracted from the Typhoon Yearbook produced by the Shanghai Typhoon Institute of the China Meteorological Administration. The latitude, longitude, minimum central pressure, and maximum surface wind speed are available every 6 h, along with landfall time and location. The direction of TC movement is determined by the change in location every 12 h. This study considers only the TCs that make landfall over mainland China, and those TCs that are not captured by any sounding data after landfall are excluded. A total of 73 TCs (including tropical depressions) from 1998 to 2009 are examined. For TCs that make landfall more than once, only the initial landfall is considered.

Surface data are gathered from 740 basic weather stations across mainland China. The sounding data are collected from the sounding stations of the World Weather Watch Global Observing System, including 120 upper-air sounding stations in China (Fig. 1). The sounding data are obtained twice daily at 11 standard pressure levels. Two sets of sounding data are used in this study. The first dataset contains data from 1950 onward, with location of the sounding balloon at the pressure level similar to that of the balloon at surface level. The other dataset provides information on the floating balloon at each pressure level from April 2003 onward. The TCs landfalling from June to September account for 87.5% of all the TCs that landed in mainland China from 2004 to 2009. We

calculate the drift distances of sounding balloons at 200 hPa from June to September of 2004–2009 (see Fig. 2). The results show that the average drift distance of the balloons over the area in which TCs typically land (south of 32°N and east of 105°E) is less than 20 km. The average drift distance at each pressure level is also computed (Fig. 3). It is found that the floating distance increases with pressure, and the maximum drift distance is 25 km at 100 hPa. This study focuses on examining the average distribution of variables (wind speed, temperature, and humidity) at each 100-km radius from the TC center, thus the drift distance of approximately 20 km has little effect on our results. To maximize the TC samples, we adopt the first sounding dataset.

## 2.2 Composite method

Obtaining sufficient sounding data to analyze the dynamical and thermodynamic structures of an individual TC is impossible; thus, most data from TCs at various time periods must be composited to determine the meaningful characteristics of their generic kinematic and thermodynamic structures. Figure 4 shows the horizontal locations of all the sample data

relative to the TC center during certain periods at 925 hPa. After discarding the sounding balloon drifting effect, the TC center locations at various pressure levels are similar to that at the surface level. Given the coarse distribution of samples, the variables are averaged azimuthally over the annular zones at each 100-km radius from the TC center. In this study, we group the sounding data every 12 h according to the snapshot time of the TC landfall. Meanwhile, the surface center of the TC at the observation time of the sounding data, namely, at 0000 and 1200 UTC, was derived from the Typhoon Yearbook.

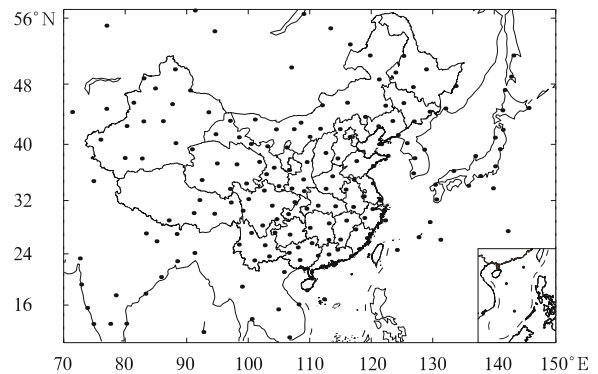


Fig. 1. Spatial distribution of the sounding stations.

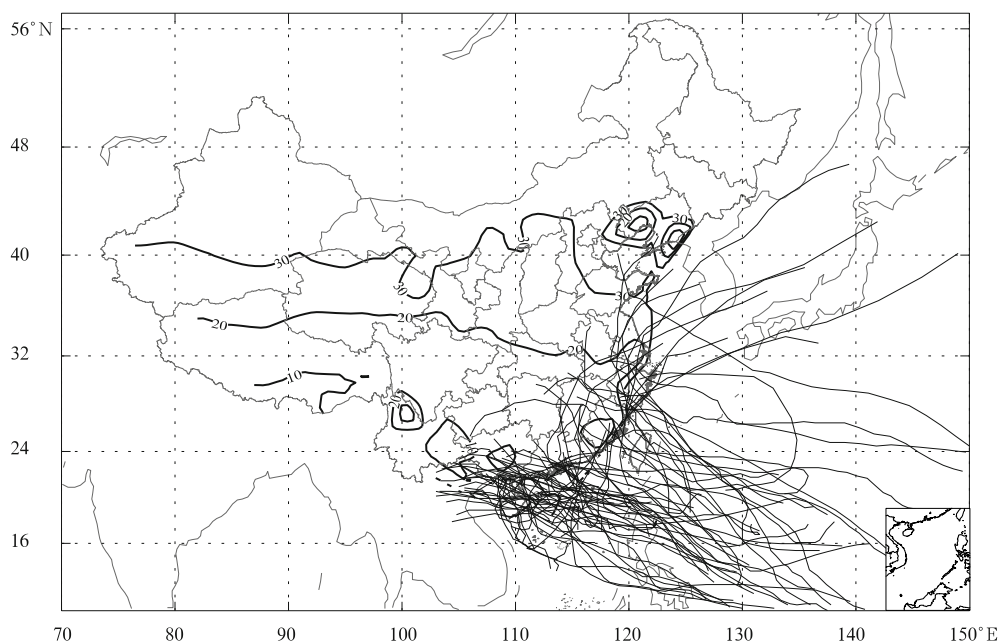
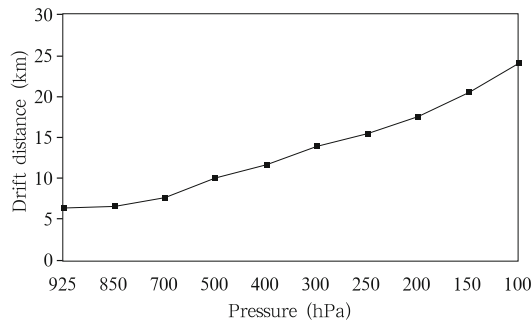


Fig. 2. Average floating distances of the sounding balloons during June–September of 2004–2009 at 200 hPa. Bold black lines indicate the drift distances, whereas thin black lines denote the tracks of landfalling TCs.



**Fig. 3.** Average drift distances of sounding balloons in the typical TC landfalling area (south of  $32^{\circ}\text{N}$  and east of  $105^{\circ}\text{E}$ ) during June–September of 2004–2009.

### 3. Kinematic structure

#### 3.1 Axisymmetric structure of a three-dimensional wind field

Figure 5 shows the azimuthal mean wind speeds of

all the sounding samples composited during the period 0–24 h before landfall and 0–72 h after landfall. The numbers of samples at each level higher than 925 hPa are nearly equal at the same radius, although they are smaller at 1000 hPa. The number of samples increases with the increase in radius. The maximum wind speed is  $17.1\text{ m s}^{-1}$  at 850 hPa and the radius is 100–200 km. Wind speed decreases at heights above 850 hPa and with radial distances farther than 100 km. This maximum wind near the top of the boundary layer has been observed in many previous studies (Franklin et al., 2003; Kepert, 2006a, b; Bell and Montgomery, 2008), which differs from the typical boundary layer under non-hurricane conditions (Zhang et al., 2011).

Similar values are derived at 0–12 h before landfall and 0–12 h, 12–24 h, and 24–36 h after landfall (Fig. 6). After landfall, the wind speed in the entire structure decreases, so is its horizontal/vertical gradi-

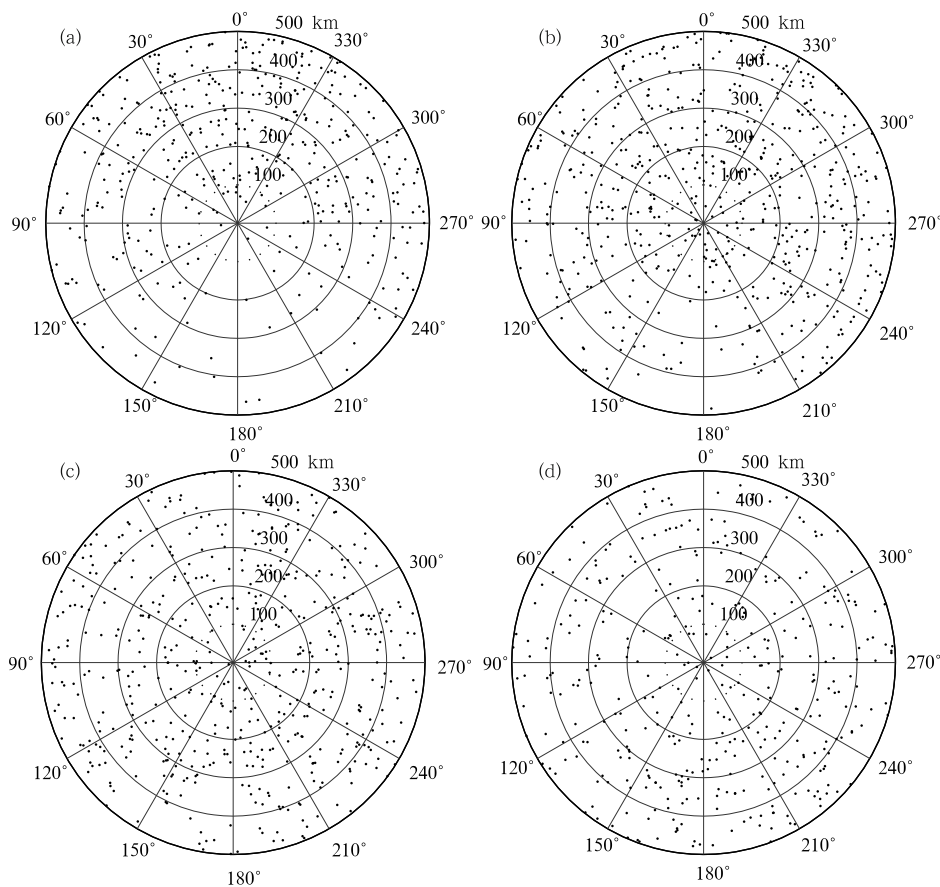


**Fig. 4.** Scatter diagrams of the samples at 925 hPa at (a) 0–12 h before landfall, (b) 0–12 h after landfall, (c) 12–24 h after landfall, and (d) 24–36 h after landfall. The direction of zero degree indicates the direction of TC movement.

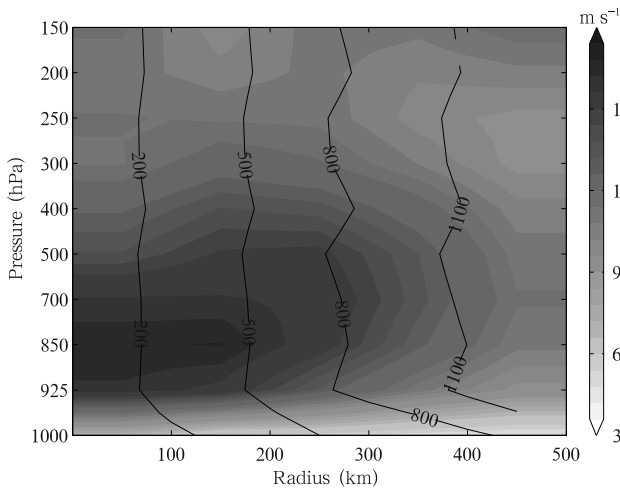


**Fig. 5.** Composite radius-pressure cross-section of azimuthal mean wind speeds (shaded;  $\text{m s}^{-1}$ ) and sample sizes (contours) from 0–24 h before landfall to 0–72 h after landfall. The shaded values are interpolated from the average wind speed at each 100-km radius.

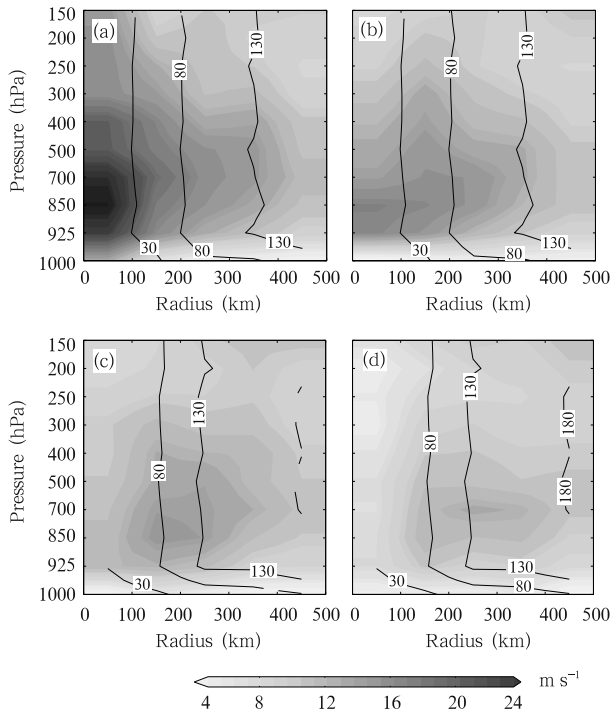


**Fig. 6.** Composite radius-pressure cross-sections of azimuthal mean wind speeds (shaded;  $\text{m s}^{-1}$ ) and sample sizes (contours) at (a) 0–12 h before landfall, (b) 0–12 h after landfall, (c) 12–24 h after landfall, and (d) 24–36 h after landfall. The shaded values are interpolated from the average wind speed at each 100-km radius.

ent. At 0–12 h after landfall, the maximum wind speed decreases sharply from 27.7 to 17.6  $\text{m s}^{-1}$ ; however, the location remains within the 100-km radius at 850 hPa. At 12–24 h after landfall, the maximum wind speed reduces to 2.1  $\text{m s}^{-1}$ , and the center location shifts to the radius between 100 and 200 km. At 24–36 h after landfall, the maximum wind speed moves outward farther from 300 to 400 km and upward to 700 hPa. This expansion of the location of maximum wind speed is also observed after the landfalls of Andy (8209) and Sepat (0709) (Chen, 1984; Li et al., 2009).

For comparison, evolution of the mean vertical profiles of horizontal wind at each 100-km radius is depicted in Fig. 7. At below 500 hPa, the mean horizontal wind within the radius of 100 km decreases most significantly after landfall and is mostly stable beyond 300 km. However, the horizontal wind at each radius begins to decay as time goes by. The wind within the 200-km radius starts to weaken within 12 h after landfall, whereas those within the 200–300-km and 400–500-km radii begin to deteriorate at 12 and 24 h post-landfall, respectively.

### 3.2 Height of the maximum wind speed

Distributions of the height of maximum wind speed ( $h_{\text{vm}}$ ) across the sounding data are given in Fig. 8. At 0–12 h before landfall, mean  $h_{\text{vm}}$  increases when the radius increases within 400 km and decreases slightly beyond this threshold (Fig. 8). This structure is also theorized and observed previously (Kepert, 2001; Schwendike and Kepert, 2008; Zhang et al., 2011). Mean  $h_{\text{vm}}$  similarly increases after the TC landfall, but the rise is slightly gentler at 24–36 h after landfall. During landfall, mean  $h_{\text{vm}}$  within the 100-km radius increases (795 and 704 hPa at 0–12 h before and 24–36 h after landfalls, respectively). Within 24 h after landfall, mean  $h_{\text{vm}}$  beyond the 100-km radius changes minimally. Although  $h_{\text{vm}}$  is widely distributed from 925 to 500 hPa, more than half of the samples are located at 850 and 925 hPa within the 100-km radius.

### 3.3 Asymmetric structure of the three-dimensional wind field

Substantial azimuthal asymmetries are often pre-

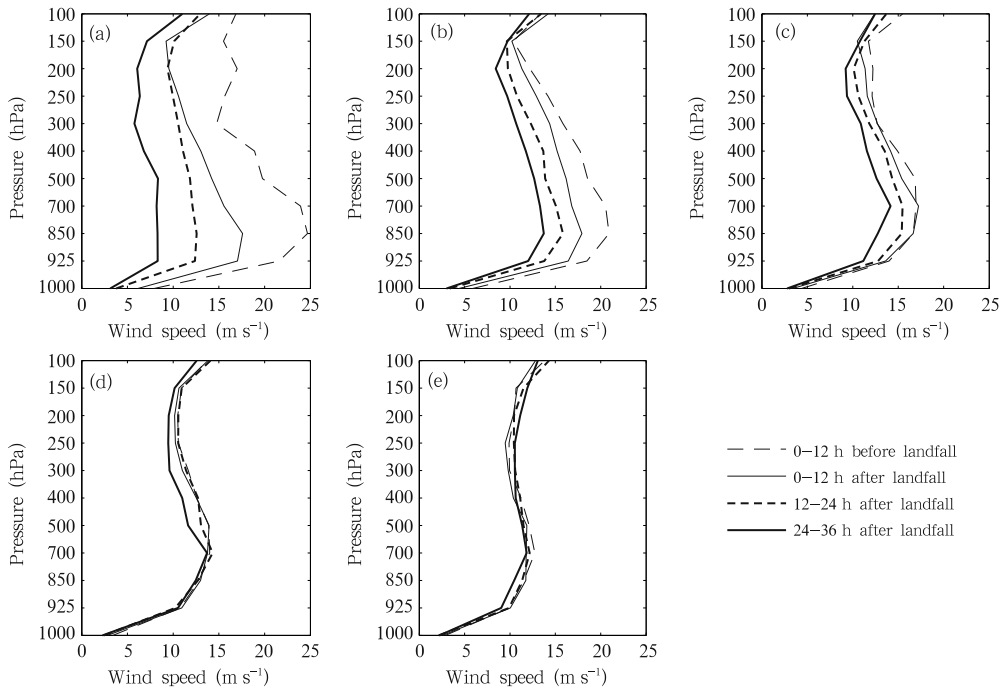


**Fig. 7.** Evolution of the mean vertical profiles of horizontal wind at radii of (a) 0–100, (b) 100–200, (c) 200–300, (d) 300–400, and (e) 400–500 km during TC landfall.

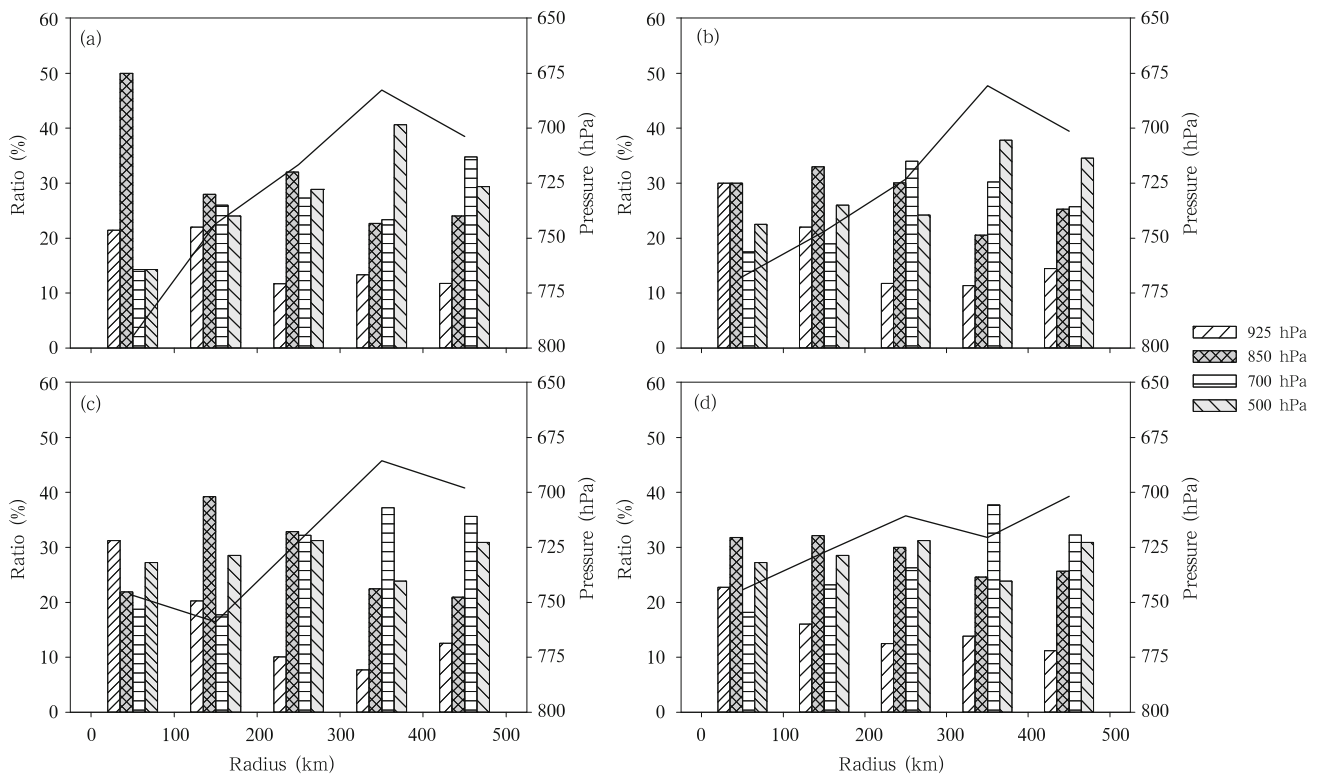


**Fig. 8.** Distributions of the height of maximum wind speed ( $h_{vm}$ ) of all the sounding data in each 100-km radius at (a) 0–12 h before landfall, (b) 0–12 h after landfall, (c) 12–24 h after landfall, and (d) 24–36 h after landfall. The bars (with  $y$ -axis labels on the left) indicate the value of  $Num_{lev}/Num_{all}$  at each 100-km radius, where  $Num_{lev}$  denotes the frequency of  $h_{vm}$  for all sounding data and  $Num_{all}$  refers to the number of sounding samples. The black lines ( $y$ -axis labels on the right) correspond to mean height.

sented in the TC wind fields, and these asymmetries vary with height in terms of amplitude and phase (Marks et al., 1992). To compute the azimuthal average, the asymmetric structure may be divided into four quadrants according to the center and the movement direction of the TC, namely, the left-front, right-front, left-rear, and right-rear quadrants.

Due to lack of data coverage over the ocean, only the wind distributions in the four quadrants following TC landfall are shown in Fig. 9. The maximum wind speed at each pressure level (except 925 hPa) is observed in the right quadrants because TC translation enhances the wind on the right side and reduces the wind on the left side. The maximum winds are closest to the TC center in the left-front quadrant and farthest in the right-rear quadrant. Wong and Chan (2007) simulated the wind distribution of a TC near its landfall, and found that the post-landfall radial inflow is weak on the right/rear-right side, and the onshore

flow was generated by the maximum wind at a large radius. During landfall, the asymmetric structure of the wind field may be the result of the combined effects of land-sea roughness, environmental flow in the background, and TC translation (Powell, 1987).

In the left-front quadrant, gale-force winds ( $> 17.1 \text{ m s}^{-1}$ ) are situated at the shallow area between 850 and 925 hPa within the 100-km radius. In the right-front quadrant, broad and strong winds with the force of a moderate gale ( $> 13.8 \text{ m s}^{-1}$ ) are produced in the deep layers. These winds are located between 925 and 400 hPa within a radius ranging from 100 to 400 km. However, only the wind at 850 hPa within a radius between 100 and 200 km achieves gale force. In the left-rear quadrant, the winds are all weaker than  $13.8 \text{ m s}^{-1}$ . In the right-rear quadrant, the gale-force winds distribute between 850 and 700 hPa at a location higher than those of the winds in other quadrants. Broad and deep winds with the force of a moderate gale spread in this area. The broadest area is located 500 km from the TC center at 700 hPa, and the deepest area is situated between 925 and 300 hPa within the 100–200-km radius.

## 4. Thermodynamic structure

### 4.1 Temperature

The composite radius-pressure cross-sections of average temperature anomalies ( $T_a$ ) before and after landfall are shown in Fig. 10.  $T_a$  is relative to the temperature that is azimuthally and radially averaged based on a radius ranging from 500 to 600 km. At 0–12 h before landfall, positive  $T_a$  within the 100-km radius is maintained through a layer whose depth ranges from 100 hPa down to 700 hPa. Between 400 and 200 hPa, a significant positive anomaly ( $T_a > 2^\circ\text{C}$ ) is observed. After landfall, the depth of the warm core is slightly shallower, with a positive value ranging from 150 to 700 hPa. However, the extent of the significant anomaly decreases sharply from 400 to 250 hPa at 0–12 h after landfall and remains at 250 hPa at 12–24 h after landfall. At 24–36 h after landfall, the positive  $T_a$  in the entire TC circulation is less than  $2^\circ\text{C}$ .

At 0–12 h before landfall, the maximum  $T_a$  is

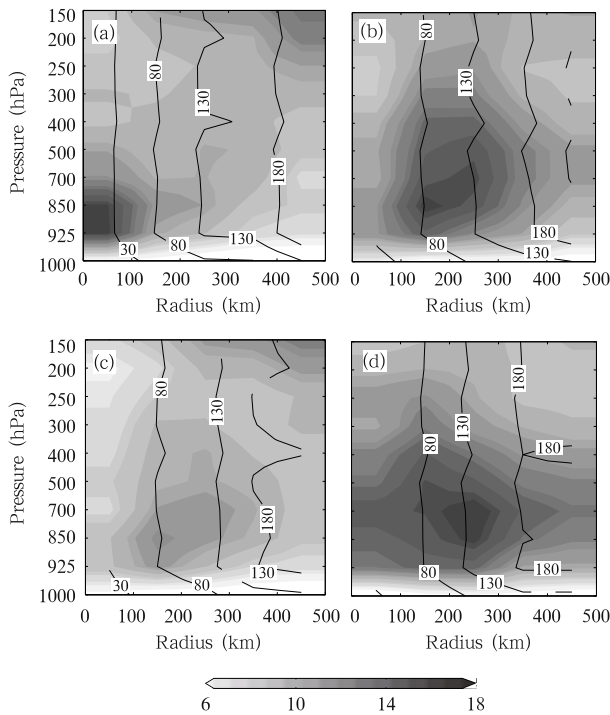


**Fig. 9.** Composites radius-pressure cross-sections of azimuthal mean wind speeds (shaded;  $\text{m s}^{-1}$ ) and sample sizes (contours) in the (a) left-front, (b) right-front, (c) left-rear, and (d) right-rear quadrants after landfall. The shaded values are interpolated from the average wind speed at each 100-km radius.

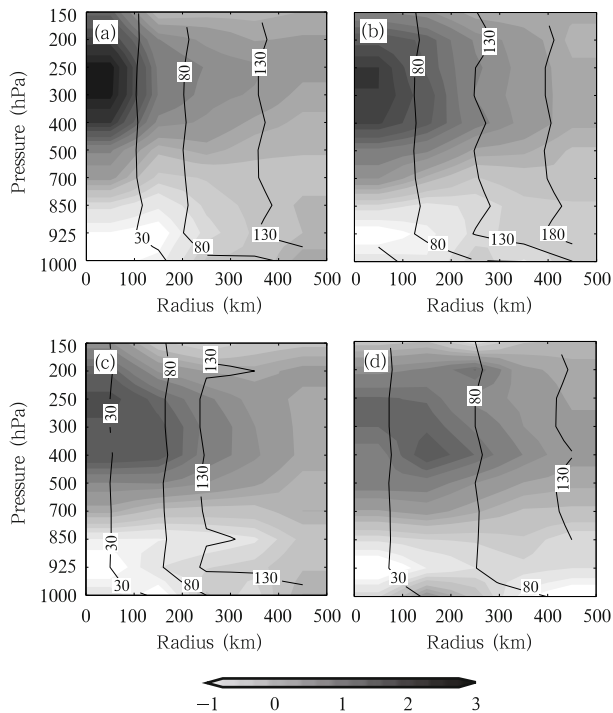


**Fig. 10.** Radius-pressure cross-sections of azimuthal mean temperature anomalies (shaded; °C) and sample sizes (contours) at (a) 0–12 h before landfall, (b) 0–12 h after landfall, (c) 12–24 h after landfall, and (d) 24–36 h after landfall. The shaded values are interpolated from the average temperature anomalies at each 100-km radius.

2.94°C at 250 hPa within a 100-km radius. After landfall,  $T_a$  and its horizontal gradient decrease significantly at above 500 hPa. At 24 h after landfall, the location of the maximum  $T_a$  remains at 250 hPa within 100 km; however, the magnitude of the maximum  $T_a$  decreases with time, especially within 12 h after landfall (Fig. 10). After 24 h, the warm core of the TC is insignificant, and the location of maximum  $T_a$  shifts to a radius between 100 and 200 km. Meanwhile, the trends of the maximum positive  $T_a$  within 100–300-km radius contradict those of the maximum positive  $T_a$  within the 100-km radius. The maximum  $T_a$  within 100–200-km (200–300-km) radius increases from 1.17°C (0.88°C) at 0–12 h before landfall to 1.79°C (1.42°C) at 24–36 h after landfall.

The distributions of  $T_a$  across different quadrants at 24 h after landfall are displayed in Fig. 11. Note that the warm TC core is insignificant 24 h post-landfall. In the four quadrants, the positive  $T_a$  within

the 100-km radius maintains through a layer with depth ranging from 100 to 700 hPa. The significant anomaly within the 100-km radius is deeper in the left- and right-front quadrants within 200–400 and 250–300 hPa, respectively. The maximum  $T_a$  in the left-front quadrant is larger than those in other quadrants at increased heights (3.11°C at 250 hPa within a 100-km radius), whereas the maximum magnitude of  $T_a$  in the left-rear quadrant is the smallest. In the right-rear quadrant, the warmest  $T_a$  is located within the 100–200-km but not the 100-km radius as in other quadrants.

#### 4.2 Relative humidity

The composite radius-pressure cross-sections of the average relative humidity (RH) before and after landfall are shown in Fig. 12. The air near low-pressure levels within a small radius is wetter than that at higher-pressure levels at a larger radius both

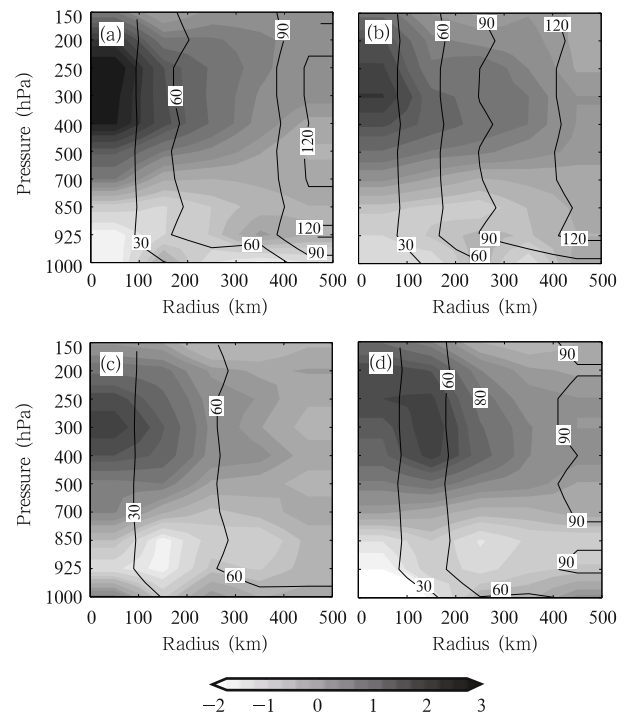


**Fig. 11.** Composite radius-pressure cross-sections of azimuthal mean temperature anomalies (shaded; °C) and sample sizes (contours) in the (a) left-front, (b) right-front, (c) left-rear, and (d) right-rear quadrants at 24 h after landfall. The shaded values are interpolated from the average temperature anomalies at each 100-km radius.

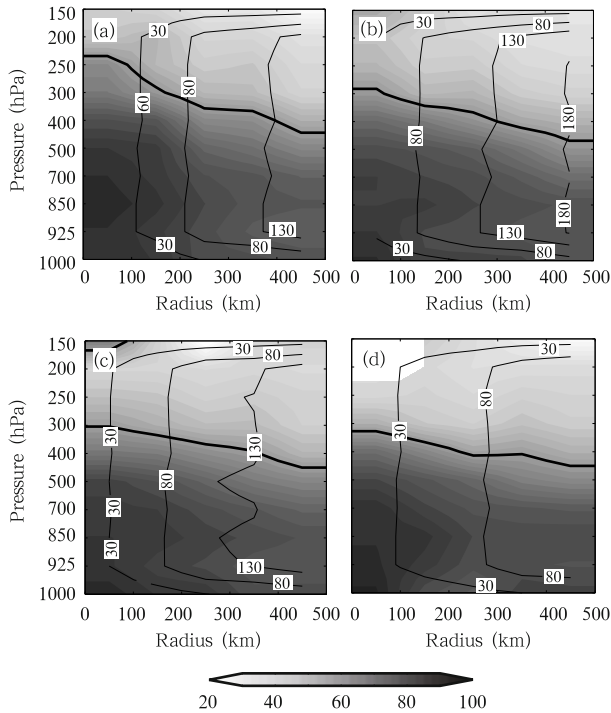


**Fig. 12.** Radius-pressure cross-sections of azimuthal mean RH (shaded; %) and sample sizes (contours) at (a) 0–12 h before landfall, (b) 0–12 h after landfall, (c) 12–24 h after landfall, and (d) 24–36 h after landfall. The shaded values are interpolated from the average RH at each 100-km radius, and the bold solid lines indicate RH = 60%.

pre- and post-TC landfall. At 0–12 h before landfall, the layers of wet air with  $\text{RH} \geq 60\%$  become shallow with the extension of the radius upward to 250 hPa within 100 km. The layers deepen to 500 hPa at the 500-km radius. After landfall, the ratio of the change with radius is smaller because the wet air layers with  $\text{RH} \geq 60\%$  are much shallower within the 100-km radius but change minimally beyond the 100-km radius. At 24–36 h after landfall, the depth of the wet air layers with  $\text{RH} \geq 60\%$  extends upward to 400 hPa from the surface within the 100-km radius.

At 0–12 h before landfall, the maximum RH is 94.2% within the 100-km radius at 850 hPa. After landfall, the location of the maxima shifts downward to 1000 hPa. The maximum values are 92.9%, 94.2%, and 95.6% at 0–12, 12–24, and 24–36 h after landfall, respectively.

After TC landfall, the air is much drier within 250–200 hPa, which is the location of the warm core,

than at the other levels within the 100-km radius. However, this phenomenon is not evident before landfall possibly because of the low-resolution data. Before TC landfall, the warm  $T_a$  at 250 hPa extends to a large radius (Fig. 10a) that can be recognized by the sounding data; whereas the dry air generated by the subsidence within the eye covers a much smaller area. After TC landfall, the warm and dry cores are clearly observed because the warm  $T_a$  and the eye expand outward.

The layers of wet air with  $\text{RH} \geq 60\%$  stretch upward from 1000 to 400 hPa in the front quadrants within the 100-km radius. These layers are shallower than those in the rear quadrants (Fig. 13). In the right-rear quadrant, the layers of wet air with  $\text{RH} \geq 90\%$  extend upward to 700 hPa within the 100-km radius, which is much deeper than those in other quadrants. In this quadrant, the maximum RH is 95.2%,

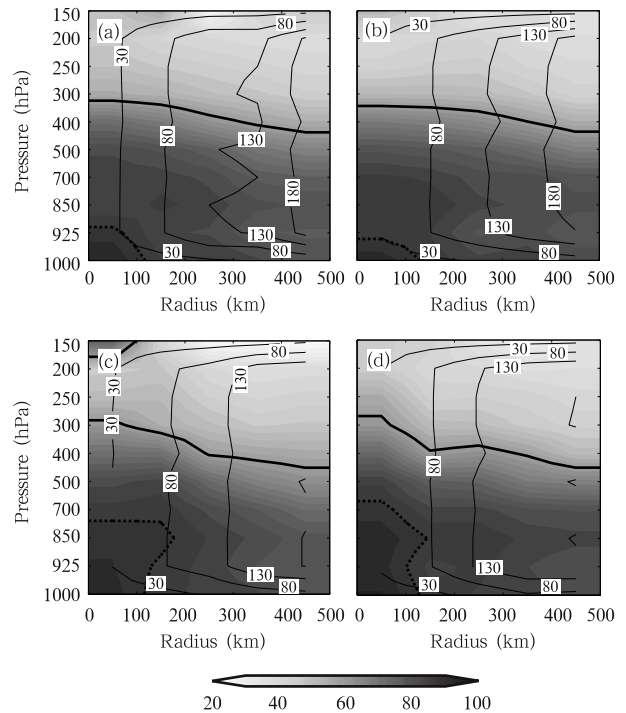


**Fig. 13.** Composite radius-pressure cross-sections of azimuthal mean RH (shaded; %) and sample sizes (contours) in the (a) left-front, (b) right-front, (c) left-rear, and (d) right-rear quadrants after landfall. The shaded values are interpolated from the average RH anomalies at each 100-km radius, the bold solid lines indicate RH = 60%, and the bold dashed lines refer to RH = 90%.

which is larger than the maxima in other quadrants.

### 4.3 Virtual potential temperature

Virtual potential temperature ( $\theta_v$ ) is an essential variable to characterize vertical stability and to determine the height of the boundary layer (Stull, 1991; Kumar et al., 2010). The variable  $\theta_v$  is calculated as in Stull (1991). In this study, we define the base of the stable layer ( $h_{\theta_v}$ ) as the lowest level with  $d\theta_v/dz \geq 3 \text{ K km}^{-1}$ . This level is taken as the mixed layer depth by Zeng et al. (2004). The lowest level at 1000 hPa is replaced by the above-surface height  $z = 10 \text{ m}$  in our computation of the vertical lapse rate of  $\theta_v$ .

Mean  $h_{\theta_v}$  generally increases with radius (Fig. 14), which is consistent with the  $h_{vm}$  trend. In contrast,  $h_{\theta_v}$  distribution differs significantly from that of  $h_{vm}$ . First, mean  $h_{\theta_v}$  varies from 922 to 860

hPa during landfall and is shallower than  $h_{vm}$  within each radius. This finding is consistent with the observational study by Zhang et al. (2011) based on the data from the global positioning system dropsondes, it is also in agreement with the model results of Ma et al. (2013). In a large radius, the differences between the means of  $h_{\theta_v}$  and  $h_{vm}$  can be observed. Second, distributions of  $h_{\theta_v}$  are highly concentrated, with over 3/4 of the samples located at 925 hPa after landfall. Third, the trend of the mean  $h_{\theta_v}$  within the 100-km radius contradicts that of  $h_{vm}$ , which decreases from 893 hPa at 0–12 h before landfall to 919 hPa at 24–36 h after landfall. This variation may be caused by their different definitions. The winds at low levels decrease more than those at higher levels because of surface friction such that the height of the maximum wind speed increases after TC landfall. After landfall, the base height of the stable layer decreases as convective

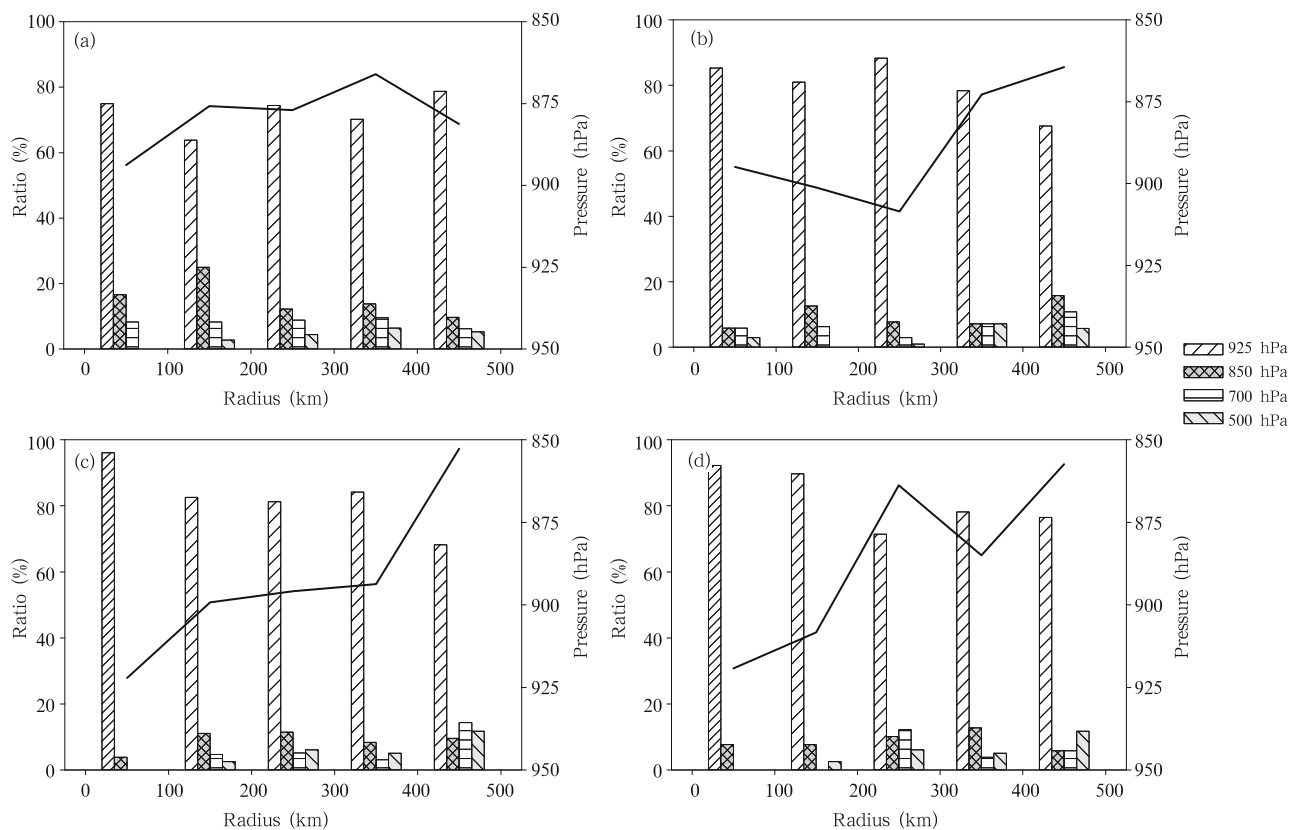


**Fig. 14.** Distributions of the base height of the stable layer defined as the lowest level of  $d\theta_v/dz \geq 3 \text{ K km}^{-1}$  at (a) 0–12 h before landfall, (b) 0–12 h after landfall, (c) 12–24 h after landfall, and (d) 24–36 h after landfall. The bars (with  $y$ -axis labels on the left) indicate the ratio of times the base of a stable layer was observed at each pressure level to all the samples at each 100-km radius, and the black lines ( $y$ -axis labels on the right) denote the mean height.

activities in TCs weaken.

## 5. Conclusions and discussion

This study examines the distribution and evolution of the wind, temperature, and humidity associated with TCs making landfall in mainland China, based on sounding data from 1998 to 2009.

Given the evolution of wind and temperature anomaly distributions every 12 h during TC landfall, we propose a general sequence of TC decay (Fig. 15). At 0–12 h after landfall, the maximum positive anomalies of wind and temperature decrease sharply; however, the locations remain unchanged. At 12–24 h after landfall, the warm core remains within 100 km, but the maximum wind speed moves outward to a large radius. After 24 h, the maximum wind speed and temperature anomalies both move farther away from the TC center. This process indicates that the maximum speed of low-level wind initially expands after landfall. As a result, the high-level warm core is damaged.

After landfall, azimuthal asymmetries in the wind field are observed. For instance, the maximum wind speed at each level (except at 925 hPa) is in the right quadrant, and it remains closest to the TC center in the left-front quadrant. By contrast, it is farthest in the right-rear quadrant. Some previous studies (e.g., Powell, 1987) reported that the asymmetric structure of the TC wind field during landfall may be generated by the combined effects of differences in land-sea

roughness, environmental flow in the background, and TC translation. These findings suggest that we must consider not only the deterioration of the entire wind structure when forecasting the wind distributions of TC after landfall, but also the asymmetries of wind speed according to radial distance, azimuthal position, and time period after landfall.

The height of the boundary layer is an essential parameter that controls the extent of the turbulent fluxes and the energy transport from the surface layer to the free atmosphere (Stull, 1991; Noh et al., 2003). With sounding data, the height of the boundary layer can be estimated based on the height of the maximum wind speed and the base of the stable layer. Although the resolution of the sounding data used in this study is too low to determine the precise depth of the boundary layer, the distributions of  $h_{vm}$  and  $h_{\theta v}$  as calculated by using the sounding data share similar features in the height of the boundary layer, according to previous studies (e.g., Zhang et al., 2011). For example, the means of  $h_{vm}$  and  $h_{\theta v}$  decrease with the closeness of the radius to the TC center within 400 km. These means drop off slightly outside the 400-km radius (Zhang et al., 2011). Other studies (e.g., Kepert, 2001) indicated that the increases in  $h_{vm}$  with radius may be related to the increase in rotational stability toward the center, whereas subsidence warming may reduce  $h_{vm}$  at a large radius (Kepert, 2010). Meanwhile, the mean of  $h_{vm}$  increases within the 100-km radius during the landfall process, and the

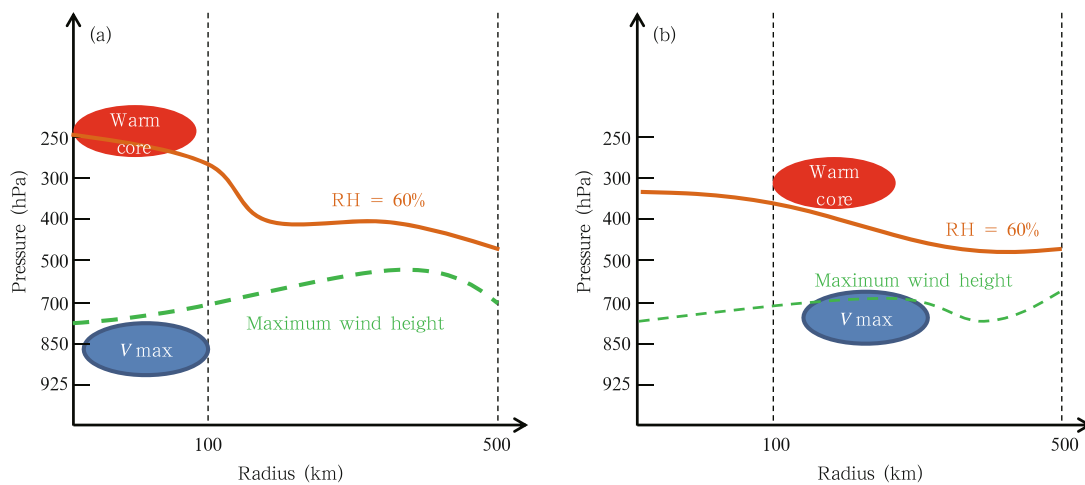


Fig. 15. Conceptual model for the TC structure at (a) 0–12 h before landfall and (b) 24–36 h after landfall.

opposite is true for the mean of  $h_{\theta v}$ . This variation may be the result of their different definitions. The winds at low levels decrease more than those at higher levels because of surface friction such that the height of the maximum wind speed increases after landfall. After landfall, the convective activities in TCs weaken, which reduces the base height of the stable layer.

These results infer the characteristics of the mean kinematic and thermodynamic structures of TCs making landfall in the mainland of China. However, further studies are required. First, the data used in this study are not fine enough; thus, case studies should be conducted on detailed TC structures using other observation data (i.e., Doppler radar data). Second, we should consider the similarities in the composition of TCs given sufficient samples, such as size, intensity, and location.

## REFERENCES

- Bell, M. M., and M. T. Montgomery, 2008: Observed structure, evolution, and potential intensity of category 5 Hurricane Isabel (2003) from 12 to 14 September. *Mon. Wea. Rev.*, **136**, 2023–2036.
- Blackwell, K. G., 2000: The evolution of Hurricane Danny (1997) at landfall: Doppler-observed eyewall replacement, vortex contraction/intensification, and low-level wind maxima. *Mon. Wea. Rev.*, **128**, 4002–4016.
- Chambers, C. R. S., and T. Li, 2011: The effect of Hawaii's big island on track and structure of tropical cyclones passing to the south and west. *Mon. Wea. Rev.*, **139**, 3609–3627.
- Chan, J. C. L., K. S. Liu, S. E. Ching, et al., 2004: Asymmetric distribution of convection associated with tropical cyclones making landfall along the South China coast. *Mon. Wea. Rev.*, **132**, 2410–2420.
- Chen Ruishan, 1984: Analysis of the features of Typhoon Andy (8209) track, intensity change and its influence of Fujian Province after its landing on Taiwan. *Marine Sci. Bull.*, **3**, 17–26. (in Chinese)
- Franklin, J. L., M. L. Black, and K. Valde, 2003: GPS dropwindsonde wind profiles in hurricanes and their operational implications. *Wea. Forecasting*, **18**, 32–44.
- Kepert, J. D., 2001: The dynamics of boundary layer jets within the tropical cyclone core. Part I: Linear theory. *J. Atmos. Sci.*, **58**, 2469–2484.
- , 2006a: Observed boundary layer wind structure and balance in the hurricane core. Part I: Hurricane Georges. *J. Atmos. Sci.*, **63**, 2169–2193.
- , 2006b: Observed boundary layer wind structure and balance in the hurricane core. Part II: Hurricane Mitch. *J. Atmos. Sci.*, **63**, 2194–2211.
- , 2010: Slab- and height-resolving models of the tropical cyclone boundary layer. Part II: Why the simulations differ. *Quart. J. Roy. Meteor. Soc.*, **136**, 1700–1711, doi: 10.1002/qj.685.
- Knupp, K. P., J. Walters, and M. Biggerstaff, 2006: Doppler profiler and radar observations of boundary layer variability during the landfall of tropical storm Gabrielle. *J. Atmos. Sci.*, **63**, 234–251.
- Kumar, M., C. Mallik, A. Kumar, et al., 2010: Evaluation of the boundary layer depth in semi-arid region of India. *Dyn. Atmos. Oceans*, **49**, 96–107.
- Li Ying, Qian Chuanhai, and Chen Lianshou, 2009: A study on the eyewall expansion of Typhoon Sepat (2009) during its landfall process. *Acta Meteor. Sinica*, **67**, 799–810. (in Chinese)
- Ma Zhanhong, Fei Jianfang, Huang Xiaogang, et al., 2013: Evaluation of the ocean feedback on height characteristics of the tropical cyclone boundary layer. *Acta Meteor. Sinica*, **27**, 910–922, doi: 10.1007/s13351-013-0611-z.
- Marks, F. D., Jr., R. A. Houze, Jr., and J. F. Gamache, 1992: Dual-aircraft investigation of the inner core of Hurricane Norbert. Part I: Kinematic structure. *J. Atmos. Sci.*, **49**, 919–942.
- Montgomery, M. T., and R. J. Kallenbach, 1997: A theory for vortex Rossby-waves and its application to spiral bands and intensity changes in hurricanes. *Quart. J. Roy. Meteor.*, **123**, 435–465.
- Noh, Y., W. G. Cheon, S. Y. Hong, et al., 2003: Improvement of the K-profile model for the planetary boundary layer based on large eddy simulation data. *Bound.-Layer Meteor.*, **107**, 401–427.
- Powell, M. D., 1987: Changes in the low-level kinematic and thermodynamic structure of Hurricane Alicia (1983) at landfall. *Mon. Wea. Rev.*, **115**, 75–99.
- , and S. H. Houston, 1998: Surface wind fields of 1995 hurricanes Erin, Opal, Luis, Marilyn, and Roxanne at landfall. *Mon. Wea. Rev.*, **126**, 1259–1273.
- Ramsay, H. A., L. M. Leslie, and J. D. Kepert, 2009: A high-resolution simulation of asymmetries in severe Southern Hemisphere tropical cyclone Larry (2006). *Mon. Wea. Rev.*, **137**, 4171–4187.

- Rebecca, S., and M. B. Gray, 2005: Low-level kinematic, thermodynamic, and reflectivity fields associated with Hurricane Bonnie (1998) at landfall. *Mon. Wea. Rev.*, **133**, 3243–3259.
- Schwendike, J., and J. D. Kepert, 2008: The boundary layer winds in hurricanes Danielle (1998) and Isabel (2003). *Mon. Wea. Rev.*, **136**, 3168–3192.
- Stull, R. B., 1991: Static stability—An update. *Bull. Amer. Meteor. Soc.*, **72**, 1521–1529.
- Szeto, K. C., and J. C. L. Chan, 2010: Structural changes of a tropical cyclone during landfall:  $\beta$ -plane simulation. *Adv. Atmos. Sci.*, **27**, 1143–1150.
- Tuleya, R. E., and Y. Kurihara, 1978: A numerical simulation of the landfall of tropical cyclones. *J. Atmos. Sci.*, **35**, 242–257.
- , M. A. Bender, and Y. Kurihara, 1984: A simulation study of the landfall of tropical cyclones. *Mon. Wea. Rev.*, **112**, 124–136.
- Wang, Y. Q., 2002: Vortex Rossby waves in a numerically simulated tropical cyclone. Part II: The role in tropical cyclone structure and intensity change. *J. Atmos. Sci.*, **59**, 1239–1262.
- Wong, M. L. M., and J. C. L. Chan, 2006: Tropical cyclone motion in response to land surface friction. *J. Atmos. Sci.*, **63**, 1324–1337.
- , and —, 2007: Modeling the effects of land-sea roughness contrast on tropical cyclone winds. *J. Atmos. Sci.*, **64**, 3249–3264.
- Zeng, X. B., M. A. Bruke, M. Y. Zhou, et al., 2004: Marine atmospheric boundary layer height over the eastern Pacific: Data analysis and model evaluation. *J. Climate*, **17**, 4159–4170.
- Zhang, J. A., R. F. Rogers, D. S. Nolan, et al., 2011: On the characteristic height scales of the hurricane boundary layer. *Mon. Wea. Rev.*, **139**, 2523–2535.